EFFECT OF A MULTI-DIMENSIONAL FLUX FUNCTION ON THE MONOTONICITY OF EULER AND NAVIER-STOKES COMPUTATIONS

A91-40705

Christopher L. Rumsey[*]
NASA Langley Research Center, Hampton VA

Bram van Leer[**]
Philip L. Roe[**]
University of Michigan, Ann Arbor, MI

ABSTRACT

A limiting method has been devised for a grid-independent flux function for use with the two-dimensional Euler and Navier-Stokes equations. This limiting is derived from a monotonicity analysis of the model and allows for solutions with reduced oscillatory behavior while still maintaining sharper resolution than a grid-aligned method. In addition to capturing oblique waves sharply, the grid-independent flux function also reduces the entropy generated over an airfoil in an Euler computation and reduces pressure distortions in the separated boundary layer of a viscous-flow airfoil computation. The model has also been extended to three dimensions, although no angle-limiting procedure for improving monotonicity characteristics has been incorporated.

INTRODUCTION

Many sophisticated numerical techniques for determining the flux at a grid interface for one-dimensional flow computations now exist. Among these is the approximate Riemann solver of Roe[1], which linearizes the system of governing equations about an average state and solves it exactly. The physics of the flow is well-represented by this method since the Riemann problem is modeled locally at each grid interface.

Unfortunately, in two or three dimensions, most flow solvers that employ any type of Riemann solver implement it in a direction-split manner, where one-dimensional theory is applied in each grid direction separately. Because of this, the advantage in sophistication of the Riemann solver is lost. In reality, the waves can travel in infinitely many directions. Constraining them to the grid directions is inconsistent with the physics of the flow and can result in improper interpretation of waves that are not aligned with the grid.

A two-dimensional grid-independent approximate Riemann solver which obtains fluxes on grid faces via wave decomposition has been developed[2,3] for use with the Euler and Navier-Stokes equations. It utilizes infor-

mation propagating in the velocity-difference direction, rather than in the grid-normal direction, so it more appropriately interprets and hence more accurately resolves shock and shear waves when they lie oblique to the grid. In reference 2, it was shown that, although oblique shock and shear waves can be captured very sharply using this method, results are also non-monotone (in the sense that oscillations and/or overshoots in flow variables such as pressure were evident near discontinuities). In the present study, a monotonicity analysis is undertaken in an effort to devise a suitable limiting procedure that will allow for sharp capturing of flowfield discontinuities with little or no nearby oscillations. Also, the grid-independent method is extended to three dimensions.

The grid-independent method uses five waves (rather than four, as in the standard grid-aligned method of Roe) to describe the difference in states at a grid face. Four of these are similar to the grid-aligned waves, except that they do not act in the grid-normal direction: two acoustic, one shear, and one entropy wave act in the direction defined by the local velocity-difference vector. The fifth wave is a shear wave which acts at a right angle to the other four. It allows for crisp representation of oblique shear waves.

The implementation of this method is nearly identical to that of the grid-aligned method. Hence it is very simple computationally to program. Since five waves are used as opposed to four, it is only slightly more costly per iteration. In practice, it is necessary to freeze the information-propagation directions partway through the computation to inhibit a nonlinear feedback which can induce oscillatory behavior in the flowfield and inhibit convergence.

---

[*] Fluid Mechanics Division, Member AIAA
[**] Professor, Member AIAA

NOMENCLATURE

A	cell area
a	speed of sound
c_x, c_y, c_z	components of unit vector
E	specific total energy
$\mathbf{F}, \mathbf{G}$	flux vectors
f	flux for scalar convection equation
H	specific total enthalpy
k	heat transfer coefficient
M	Mach number
$\vec{n}$	unit direction vector
p	pressure
$\dot{Q}_i$	heat flux terms
q	normal velocity
$\mathbf{R}$	wave vectors
Re	Reynolds number
r	parallel velocity
T	temperature
t	time
$\mathbf{U}$	conserved variables
u, v, w	components of velocity
$\bar{u}_s$	drift velocity of shear wave
$\vec{V}$	velocity
x, y, z	Cartesian coordinates
$y_{1,\ldots,12}$	parameters defining allowable θ'_d
α	angle-of-attack, or flow angle
β	free parameter in 5-wave model
γ	ratio of specific heats, taken as 1.4
$\Delta r_{1,2,3}$	differences defined by equation (46)
Δs	cell face length
θ, ψ	angular directions
Λ	matrix of wavespeeds
λ	wavespeed component in grid direction; also second coefficient of viscosity
μ	coefficient of viscosity
ρ	density
τ_{ij}	viscous shear stress terms
Φ	flux per unit length
ϕ_p	angle between planes
Ω	vector of wavestrengths

Subscripts:

d	velocity-difference direction
f	flow direction
g	grid-normal direction
i, j	grid indices
L, R	from the left, right
v	viscous

Superscripts:

$\wedge$	Roe-averaged
$*$	associated with θ'_d-direction
$**$	associated with $(\theta'_d + \pi/2)$-direction
$'$	indicates frozen direction

TWO-DIMENSIONAL MODEL

Governing Equations and Numerical Method

The two-dimensional Navier-Stokes equations can be written as

$$\frac{\partial \mathbf{U}}{\partial t} + \frac{\partial \mathbf{F}}{\partial x} + \frac{\partial \mathbf{G}}{\partial y} = \frac{\partial \mathbf{F_v}}{\partial x} + \frac{\partial \mathbf{G_v}}{\partial y}, \qquad (1)$$

where the conserved variables are $\mathbf{U} = [\rho, \rho u, \rho v, \rho E]^T$ and the inviscid flux vectors are

$$\mathbf{F} = \begin{bmatrix} \rho u \\ \rho u^2 + p \\ \rho uv \\ \rho uH \end{bmatrix} \qquad \mathbf{G} = \begin{bmatrix} \rho v \\ \rho uv \\ \rho v^2 + p \\ \rho vH \end{bmatrix}. \qquad (2)$$

The viscous fluxes are

$$\mathbf{F_v} = \begin{bmatrix} 0 \\ \tau_{11} \\ \tau_{21} \\ u_j \tau_{1j} + k\frac{\partial T}{\partial x} \end{bmatrix} \qquad \mathbf{G_v} = \begin{bmatrix} 0 \\ \tau_{12} \\ \tau_{22} \\ u_j \tau_{2j} + k\frac{\partial T}{\partial y} \end{bmatrix}, \qquad (3)$$

where

$$\tau_{ij} = \mu\left(\frac{\partial u_i}{\partial x_j} + \frac{\partial u_j}{\partial x_i}\right) + \lambda\frac{\partial u_k}{\partial x_k}\delta_{ij}, \qquad (4)$$

and λ is taken as $-(2/3)\mu$ (Stokes' hypothesis). The ideal gas equation-of-state closes the set of equations:

$$p = (\gamma - 1)\rho\left[E - \frac{u^2 + v^2}{2}\right]. \qquad (5)$$

The equations can be discretized in finite volume form as

$$\frac{\partial \mathbf{U}_{i,j}}{\partial t} = -\frac{1}{A_{i,j}}\left\{\sum_{\ell=1}^{4}\Phi_\ell \Delta s_\ell - \sum_{\ell=1}^{4}(\Phi_v)_\ell \Delta s_\ell\right\}_{i,j} \qquad (6)$$

$$\Phi = \begin{bmatrix} \rho q_g \\ \rho q_g u + p\cos\theta_g \\ \rho q_g v + p\sin\theta_g \\ \rho q_g H \end{bmatrix} \qquad (7)$$

$$\Phi_v = \begin{bmatrix} 0 \\ \tau_{11}\cos\theta_g + \tau_{12}\sin\theta_g \\ \tau_{21}\cos\theta_g + \tau_{22}\sin\theta_g \\ (V_j\tau_{1j} - \dot{Q}_1)\cos\theta_g + (V_j\tau_{2j} - \dot{Q}_2)\sin\theta_g \end{bmatrix}, \qquad (8)$$

where θ_g is the angle that the outward-pointing cell face normal makes with the x-axis, and q_g is the outward velocity normal to the cell face, given by

$$q_g \equiv u\cos\theta_g + v\sin\theta_g. \qquad (9)$$

Here, $\Phi_\ell \Delta s_\ell$ is the inviscid normal flux at cell face ℓ, evaluated through the use of either a grid-aligned or grid-independent flux function. The term $(\Phi_v)_\ell \Delta s_\ell$ is the viscous normal flux at cell face ℓ, evaluated using central differencing.

A summary of the two-dimensional grid-independent flux function is given here. Full details of the derivation can be found in references 2 and 3. The flux per unit face length is written as

$$\Phi = \frac{1}{2}\left(\Phi_L + \Phi_R\right) - \frac{1}{2}\sum_{k=1}^{5}|\hat{\lambda}_k|\hat{\Omega}_k\hat{R}_k, \qquad (10)$$

where the five waves are given by

$$\hat{R}_1 = \left[1, \hat{u} + \hat{a}\cos\theta'_d, \hat{v} + \hat{a}\sin\theta'_d, \hat{H} + \hat{a}\hat{q}'_d\right]^T$$

$$\hat{R}_2 = \left[1, \hat{u} - \hat{a}\cos\theta'_d, \hat{v} - \hat{a}\sin\theta'_d, \hat{H} - \hat{a}\hat{q}'_d\right]^T$$

$$\hat{R}_3 = \left[0, -\hat{a}\cos\theta'_d, -\hat{a}\sin\theta'_d, -\hat{a}\hat{q}'_d\right]^T \qquad (11)$$

$$\hat{R}_4 = \left[1, \hat{u}, \hat{v}, \frac{1}{2}(\hat{u}^2 + \hat{v}^2)\right]^T$$

$$\hat{R}_5 = \left[0, -\hat{a}\sin\theta'_d, \hat{a}\cos\theta'_d, \hat{a}\hat{r}'_d\right]^T.$$

Hats denote Roe-averaged variables, as defined in reference 1. The five equations in (11) represent, respectively: $+\theta'_d$ acoustic, $-\theta'_d$ acoustic, $(\theta'_d + \frac{\pi}{2})$ shear, θ'_d entropy, and θ'_d shear waves. The velocity-difference direction $\theta_d = \tan^{-1}(\Delta v / \Delta u)$, where $\Delta(\cdot) \equiv (\cdot)_R - (\cdot)_L$, defines the primary direction of assumed wave propagation at each interface. It is frozen as θ'_d at some point during the computation in order to avoid nonlinear feedback in the solution. The variables $\hat{q}'_d$ and $\hat{r}'_d$ are defined by

$$\hat{q}'_d \equiv \hat{u}\cos\theta'_d + \hat{v}\sin\theta'_d$$
$$\hat{r}'_d \equiv -\hat{u}\sin\theta'_d + \hat{v}\cos\theta'_d. \qquad (12)$$

The kth wave of this system has a strength $\hat{\Omega}_k$, evaluated as the kth component of the vector $\hat{\Omega}$, where

$$\hat{\Omega} = \begin{bmatrix} \frac{\Delta p}{2\hat{a}^2} + \beta\frac{\hat{\rho}}{2\hat{a}}\left(\Delta u\cos\theta'_d + \Delta v\sin\theta'_d\right) \\ \frac{\Delta p}{2\hat{a}^2} - \beta\frac{\hat{\rho}}{2\hat{a}}\left(\Delta u\cos\theta'_d + \Delta v\sin\theta'_d\right) \\ (\beta - 1)\frac{\hat{\rho}}{\hat{a}}\left(\Delta u\cos\theta'_d + \Delta v\sin\theta'_d\right) \\ \frac{1}{\hat{a}^2}\left(\hat{a}^2\Delta\rho - \Delta p\right) \\ \frac{\hat{\rho}}{\hat{a}}\left(-\Delta u\sin\theta'_d + \Delta v\cos\theta'_d\right) \end{bmatrix}, \qquad (13)$$

The components of the wavespeeds in the grid direction are

$$\hat{\lambda}_1 = (\hat{q}'_d + \hat{a})\cos(\theta'_d - \theta_g)$$
$$\hat{\lambda}_2 = (\hat{q}'_d - \hat{a})\cos(\theta'_d - \theta_g)$$
$$\hat{\lambda}_3 = \hat{r}'_d\{-\sin(\theta'_d - \theta_g)\} \qquad (14)$$
$$\hat{\lambda}_4 = \hat{q}'_d\cos(\theta'_d - \theta_g)$$
$$\hat{\lambda}_5 = \hat{q}'_d\cos(\theta'_d - \theta_g).$$

The parameter β determines the strength of the $(\theta'_d + \frac{\pi}{2})$ shear wave relative to the acoustic waves. The current method for determining β is due to Parpia[4] and is derived in reference 3. It is defined by: $\beta \equiv$

$$\min\left[\max\left\{\left(\frac{\Delta p/(\hat{\rho}\hat{a})}{\Delta u\cos\theta'_d + \Delta v\sin\theta'_d}\right)^2, .05\right\}, 1\right], \qquad (15)$$

and is generally frozen along with θ'_d as an aid to convergence.

This flux function has been used both in conjunction with an explicit m-stage finite-volume upwind scheme as well as with an implicit finite-volume upwind approximate-factorization (A-F) scheme (CFL2D[5]). A stability analysis given in reference 2 of the explicit scheme showed the method to be stable in conjunction with $m = 2$ or more stages (with appropriately chosen coefficients). A stability analysis of the implicit A-F method for the Euler equations, given in reference 3, indicates a practical stability limit of about 4 for the CFL number for first-order spatial differencing and about 2 for second-order when grid-aligned approximate left-hand side Jacobians are employed.

Monotonicity Analysis

The method for analyzing the monotonicity of the two-dimensional Euler equations is derived from considerations of the scalar convection equation $u_t + au_x = 0$. The results of the Euler equations analysis are considered to be valid for the Navier-Stokes equations as well, since the viscous terms add dissipation which tends to mitigate numerical oscillations that may occur near regions of high gradient.

The one-dimensional scalar convection equation is written in finite-volume form, with forward-Euler time stepping (i is a given cell bordered by $(i-1)$ to the left and $(i+1)$ to the right):

$$u_i^{n+1} = u_i^n - \frac{\Delta t}{\Delta x}\left(f_{i+\frac{1}{2}} - f_{i-\frac{1}{2}}\right). \qquad (16)$$

Here $f_{i+1/2}$ and $f_{i-1/2}$ are flux functions on the $(i+1/2)$ and $(i-1/2)$ cell faces, respectively, and Δx is the distance between the gridpoints. Consider now a computational stencil in which u_i^{n+1} only depends on u_i^n, u_{i+1}^n, and u_{i-1}^n. Godunov[6] showed that one way to insure that spurious oscillations do not develop is to require that variations in u in each neighboring cell causes a variation *in the same direction* in cell i. In other words, if u_{i-1} increases, then u_i should also increase, or at worst remain unchanged. A similar requirement holds for changes in the $(i+1)$ cell. These requirements can be written

$$\frac{\partial u_i^{n+1}}{\partial u_{i+1}^n} \geq 0 \qquad \text{and} \qquad \frac{\partial u_i^{n+1}}{\partial u_{i-1}^n} \geq 0 \qquad (17)$$

or, since $f_{i+1/2}$ is identical to $f(u_{i+1}, u_i)$ and $f_{i-1/2}$ is identical to $f(u_i, u_{i-1})$,

$$\frac{\partial f_{i+\frac{1}{2}}}{\partial u_{i+1}} \leq 0 \quad \text{and} \quad \frac{\partial f_{i-\frac{1}{2}}}{\partial u_{i-1}} \geq 0. \tag{18}$$

A third restriction is $\partial u_i^{n+1}/\partial u_i^n \geq 0$, but this merely limits the time step.

As an example, consider first-order upwind differencing, which is already known to be monotone:

$$f_{i+\frac{1}{2}} = \frac{1}{2}a(u_{i+1} + u_i) - \frac{1}{2}|a|(u_{i+1} - u_i)$$
$$f_{i-\frac{1}{2}} = \frac{1}{2}a(u_i + u_{i-1}) - \frac{1}{2}|a|(u_i - u_{i-1}). \tag{19}$$

Here, $\partial f_{i+1/2}/\partial u_{i+1} = \frac{1}{2}(a - |a|)$, which is non-positive, and $\partial f_{i-1/2}/\partial u_{i-1} = \frac{1}{2}(a + |a|)$, which is non-negative. Hence first-order upwind differencing satisfies (18), as expected. A counter-example is central-differencing, which is already known *not* to be monotone:

$$f_{i+\frac{1}{2}} = \frac{1}{2}a(u_{i+1} + u_i)$$
$$f_{i-\frac{1}{2}} = \frac{1}{2}a(u_i + u_{i-1}). \tag{20}$$

Here, it is seen that (18) can never be satisfied except for the degenerate case of $a = 0$, since both $\partial f_{i+1/2}/\partial u_{i+1}$ and $\partial f_{i-1/2}/\partial u_{i-1} = \frac{1}{2}a$.

In order to analyze the two-dimensional Euler equations in conjunction with the 5-wave model, they are written in finite-volume form with forward-Euler time stepping, and it is assumed for simplicity that the mesh is made up of square cells:

$$\mathbf{U}_{i,j}^{n+1} = \mathbf{U}_{i,j}^n - \frac{\Delta t}{\Delta s}\Big(\mathbf{\Phi}_{i+\frac{1}{2},j} - \mathbf{\Phi}_{i-\frac{1}{2},j} + \mathbf{\Phi}_{i,j+\frac{1}{2}} - \mathbf{\Phi}_{i,j-\frac{1}{2}} \Big), \tag{21}$$

It is further assumed that the computational stencil is made up of only (i,j), $(i+1,j)$, $(i-1,j)$, $(i,j+1)$, and $(i,j-1)$, so that in one time step $\mathbf{U}_{i,j}$ is only a function of its initial value and the values in the four immediate neighboring cells. This is a spatially first-order accurate scheme.

Now, instead of one equation, there are four coupled equations, and the quantities $\partial \mathbf{U}_{i,j}^{n+1}/\partial \mathbf{U}_k^n$, where $k = (i+1,j)$, $(i-1,j)$, $(i,j+1)$, $(i,j-1)$, are not single variables but 4×4 matrices. The four eigenvalues of each of these matrices represent the change of four *local* characteristic variables at (i,j) with respect to the change in those same variables in the corresponding neighboring cell. Since the equations are decoupled with respect to these local characteristic variables, nonnegative eigenvalues imply a type of monotonicity property. This property is utilized to help define a limiting

procedure for reducing oscillations in two-dimensional solutions.

The conditions equivalent to (17) for the Euler equations are

$$\text{e.v.}\left(\frac{\partial \mathbf{U}_{i,j}^{n+1}}{\partial \mathbf{U}_k^n} \right) \geq 0 \tag{22}$$

for $k = (i+1,j), (i-1,j), (i,j+1), (i,j-1)$, or, equivalently,

$$\text{e.v.}\left(\frac{\partial \mathbf{\Phi}_{i+\frac{1}{2},j}}{\partial \mathbf{U}_{i+1,j}} \right) \leq 0 \quad \text{e.v.}\left(\frac{\partial \mathbf{\Phi}_{i,j+\frac{1}{2}}}{\partial \mathbf{U}_{i,j+1}} \right) \leq 0$$
$$\text{e.v.}\left(\frac{\partial \mathbf{\Phi}_{i-\frac{1}{2},j}}{\partial \mathbf{U}_{i-1,j}} \right) \geq 0 \quad \text{e.v.}\left(\frac{\partial \mathbf{\Phi}_{i,j-\frac{1}{2}}}{\partial \mathbf{U}_{i,j-1}} \right) \geq 0, \tag{23}$$

where e.v.$(\cdot)$ represents "the eigenvalues of $(\cdot)$". If the grid-normal angle θ_g is varied over the full range of possible angles, then satisfying all four inequalities in (23) is redundant. Satisfying the two inequalities on opposing faces (say the $(i+1/2,j)$ face and the $(i-1/2,j)$ face) is then sufficient to insure this monotonicity property.

In order to proceed with the monotonicity analysis for the 5-wave grid-independent model, write (10) in slightly different form:

$$\mathbf{\Phi}_{i+\frac{1}{2},j} = \frac{1}{2}\big(\mathbf{\Phi}_{i+1,j} + \mathbf{\Phi}_{i,j} \big) - \frac{1}{2}\big\{ [\hat{\mathbf{R}}^*][\hat{\mathbf{\Lambda}}^*]\cos(\theta_d' - \theta_g)|\hat{\mathbf{\Omega}}^* + [\hat{\mathbf{R}}^{**}][\hat{\mathbf{\Lambda}}^{**}](-\sin(\theta_d' - \theta_g))|\hat{\mathbf{\Omega}}^{**} \big\}. \tag{24}$$

$[\hat{\mathbf{R}}^*]$ is the matrix of wave vectors acting in the θ_d'-direction ($\hat{\mathbf{R}}_{1,2,4,5}$ in (11)). $[\hat{\mathbf{R}}^{**}]$ is the corresponding matrix of wave vectors acting in the $(\theta_d' + \frac{\pi}{2})$-direction (only the shear vector, $\hat{\mathbf{R}}_3$ in (11), is used in the 5-wave model). Then $[\hat{\mathbf{\Lambda}}^*] = \text{diag}(\hat{q}_d' + \hat{a}, \hat{q}_d' - \hat{a}, \hat{q}_d', \hat{q}_d')$ and $[\hat{\mathbf{\Lambda}}^{**}] = \text{diag}(\hat{r}_d' + \hat{a}, \hat{r}_d' - \hat{a}, \hat{r}_d', \hat{r}_d')$ are the corresponding wavespeeds in those same directions. The wavestrengths, taken from (13), in the two directions are

$$\hat{\mathbf{\Omega}}^* = \begin{bmatrix} \frac{\Delta p}{2\hat{a}^2} + \beta\frac{\hat{\rho}}{2\hat{a}}\left(\Delta u\cos\theta_d' + \Delta v\sin\theta_d'\right) \\ \frac{\Delta p}{2\hat{a}^2} - \beta\frac{\hat{\rho}}{2\hat{a}}\left(\Delta u\cos\theta_d' + \Delta v\sin\theta_d'\right) \\ \frac{1}{\hat{a}^2}\left(\hat{a}^2\Delta\rho - \Delta p\right) \\ \frac{\hat{\rho}}{\hat{a}}\left(-\Delta u\sin\theta_d' + \Delta v\cos\theta_d'\right) \end{bmatrix} \tag{25}$$

$$\hat{\mathbf{\Omega}}^{**} = \begin{bmatrix} 0 \\ 0 \\ 0 \\ (\beta - 1)\frac{\hat{\rho}}{\hat{a}}\left(\Delta u\cos\theta_d' + \Delta v\sin\theta_d'\right) \end{bmatrix}. \tag{26}$$

The present study concentrates on the variations in $\hat{\mathbf{\Omega}}^*$ and $\hat{\mathbf{\Omega}}^{**}$. It is assumed that the wave vectors, wavespeeds, and θ_d' are constant, and all variables are taken as the Roe-averaged values. Therefore this is a

linearized analysis. With these assumptions, one can obtain

$$\frac{\partial \Phi_{i+\frac{1}{2},j}}{\partial \mathbf{U}_{i+1,j}} = \frac{1}{2}\frac{\partial \hat{\Phi}}{\partial \mathbf{U}}(\theta_g) -$$

$$\frac{1}{2}\left\{ [\hat{\mathbf{R}}^*][\hat{\Lambda}^*]\cos(\theta_d' - \theta_g)|\frac{\partial \hat{\Omega}^*}{\partial \mathbf{U_R}} + \right. \tag{27}$$

$$\left. [\hat{\mathbf{R}}^{**}][\hat{\Lambda}^{**}](-\sin(\theta_d' - \theta_g))|\frac{\partial \hat{\Omega}^{**}}{\partial \mathbf{U_R}} \right\}$$

along with a similar expression for $\partial \Phi_{i-1/2,j}/\partial \mathbf{U}_{i-1,j}$. The derivative matrices $\partial \hat{\Omega}^*/\partial \mathbf{U_R}$ and $\partial \hat{\Omega}^{**}/\partial \mathbf{U_R}$ are obtained in a straightforward fashion from (25) and (26). The monotonicity constraints are

$$\begin{aligned} \text{e.v.}\left(\frac{\partial \Phi_{i+\frac{1}{2}}}{\partial \mathbf{U}_{i+1}}\right) &\le 0 \\ \text{e.v.}\left(\frac{\partial \Phi_{i-\frac{1}{2}}}{\partial \mathbf{U}_{i-1}}\right) &\ge 0. \end{aligned} \tag{28}$$

The monotonicity analysis is carried out numerically. The Mach number M, flow angle α, and β are chosen, then θ_g and θ_d' are each varied independently between $-90°$ and $90°$ with incremental changes of $\pi/32$. Eigenvalues are computed for each condition. If they meet the criteria of equation (28), then monotonicity is preserved at that condition. It turns out that plotting $(\theta_d' - \alpha)$ vs. $(\theta_g - \alpha)$ removes the dependence on α (in other words, plots are the same regardless of the value of α).

A sample plot is shown in figure 1(a). The conditions are M = 3, β = 0.95. There are two very small regions where monotonicity is preserved. (Note that some points may be missing from these monotonicity plots wherever the eigenvalue solver does not converge within a specified number of iterations. However, we are more interested in general regions than in specific points.) As a specific example, from the figure it is seen that the scheme is monotone for approximately $30° < \theta_d' - \alpha < 75°$ when $\theta_g - \alpha = 75°$. This allowable θ_d' region is sketched in figure 1(b).

It is also evident from figure 1(a) that if $(\theta_g - \alpha)$ lies between roughly $-60°$ and $60°$, then no θ_d' chosen will insure monotonicity. Other β's less than 1.0 produce similar plots. Only when $\beta = 1.0$ is there always *some* θ_d' that will yield a monotone scheme, as demonstrated in figure 2(a). Here, the diagonal where $\theta_d' = \theta_g$ corresponds to the grid-aligned scheme. The effect of Mach number is shown in figures 2(b) and (c) for $\beta = 1.0$. At low Mach numbers, only the grid-aligned method is monotone (i.e. θ_d' must $= \theta_g$ and β must $= 1.0$), while at higher supersonic Mach numbers the monotone region is extended slightly from the M = 3 case.

It is clear from this analysis that the restrictions on allowable θ_d' for a monotone scheme given by this analysis are quite severe, if not impossible to meet. Fortunately, in practice it appears that the restrictions on θ_d'

can be relaxed somewhat while still maintaining reasonably non-oscillatory solutions near discontinuities for a wide variety of flows.

Through extensive numerical experimentation, the following observations have been made regarding reducing the oscillatory behavior of the grid-independent model to an acceptable level: (1) When M > 1 best results are obtained when θ_d' is limited to lie between $\alpha + K*\text{sign}(\theta_g - \alpha)$ and θ_g. K is a small number for lower Mach numbers and is larger for higher Mach numbers. (2) When M $\ll 1$ θ_d' does not need to be restricted, except in a very small region (see (3) below). Between M = 0 and M = 1 best results are obtained if the allowable region transitions smoothly between the subsonic and supersonic cases. (3) In the boundary layer region of Navier-Stokes solutions, odd-even point decoupling can occur when θ_d' is taken as $(\theta_g \pm \frac{\pi}{2})$ and $\alpha \approx \theta_d'$. This condition occurs on grid interfaces in the boundary layer that are aligned with the flow direction, and is due to the fact that all components of the θ_d'-wavespeeds in the grid direction equal zero and the $(\theta_d' + \frac{\pi}{2})$ shear wave has an extremely small wavespeed. Hence the dissipation is very small and the result is essentially central-differencing in that direction. By limiting the angle θ_d' to lie outside of a small region near $(\theta_d' - \alpha) = 0$ at $(\theta_g - \alpha) = \pm 90°$, this decoupling can be alleviated. Numerical examples of viscous flows both with and without θ_d'-limiting will be given in the Results section.

An attempt has been made to parameterize the "monotonicity regions" in accordance with the three observations made above. The empirically-generated θ_d'-limited regions for four different Mach numbers are shown in figures 3(a) through (d). It should be stressed that the determination of these regions is based only loosely on theory and primarily on numerical experimentation. The following empirical scheme has been found to give good results for a wide variety of problems. It is by no means deemed to be the best scheme for improving the monotonicity properties of the 5-wave model. First, some variables are defined:

$$y_1 \equiv \frac{(\theta_g - \alpha) + \pi/2}{1 - \min(M,1)^4 + 0.01} \tag{29}$$

$$y_2 \equiv \frac{(\theta_g - \alpha) - \pi/2}{1 - \min(M,1)^4 + 0.01} \tag{30}$$

$$y_3 \equiv -\frac{\pi}{8}\left\{\tanh\left(\frac{M-20}{12}\right) + 1\right\} \tag{31}$$

$$y_4 \equiv \frac{\pi}{8}\left\{\tanh\left(\frac{M-20}{12}\right) + 1\right\} \tag{32}$$

$$y_5 \equiv (\theta_g - \alpha) + \frac{\pi}{2} - \frac{\pi}{2}\min(M,1)^4 \tag{33}$$

$$y_6 \equiv (\theta_g - \alpha) - \frac{\pi}{2} + \frac{\pi}{2}\min(M,1)^4 \tag{34}$$

$$y_7 \equiv +\sqrt{\max\left[\left(\frac{\pi}{9}\right)^2 - \left\{(\theta_g - \alpha) + \frac{\pi}{2}\right\}^2, 0\right]} \tag{35}$$

$$y_8 \equiv -y_7 \tag{36}$$

$$y_9 \equiv +\sqrt{\max\left[\left(\frac{\pi}{9}\right)^2 - \left\{(\theta_g - \alpha) - \frac{\pi}{2}\right\}^2, 0\right]} \tag{37}$$

$$y_{10} \equiv -y_9 \tag{38}$$

$$y_{11} \equiv \min\left(y_6, \max(y_4, y_9)\right) \tag{39}$$

$$y_{12} \equiv \max\left(y_5, \min(y_3, y_8)\right). \tag{40}$$

The allowable regions are then taken as:

$$
\begin{aligned}
(\theta'_d - \alpha) &> \max(y_1, y_7) \\
(\theta'_d - \alpha) &< \min(y_2, y_{10}) \\
y_{11} &< (\theta'_d - \alpha) < y_{12}.
\end{aligned} \tag{41}
$$

If $(\theta'_d - \alpha)$ does not lie within one of the allowable regions, then it is limited to either y_{11} or y_{12}, whichever is closer.

Results and Discussion

A first-order Euler computation of supersonic channel flow with a 15° finite-length ramp is computed at an inflow Mach number of 2.0 on a 49 × 17 grid. (This case was first used to test grid-independent flow solvers by Levy et. al.[7]) Figures 4(a) through (c) show Mach contours and Mach number values along j=constant cuts for the grid-aligned scheme, the 5-wave model (θ'_d-unlimited), and the 5-wave model (θ'_d-limited). The unlimited grid-independent method yields extremely sharp shocks, but many oscillations are evident in the flowfield. The limited method reduces the oscillations while still providing more resolution than the grid-aligned scheme.

An unexpected advantage of the grid-independent model over the grid-aligned scheme turns up during the course of a grid convergence study using the Euler equations to solve subsonic flow over an airfoil. Figure 5 is a plot of computed drag coefficient vs. the inverse of the square root of the grid density for the grid-aligned scheme and the 5-wave model on three different grids for M = 0.3 and $\alpha = 1°$, using first-order spatial discretization. The finest grid is a 257 × 73 O-mesh with average minimum spacing on the body of 0.0031c and maximum grid extent of 20c. Coarser meshes are achieved by removing every other point from the next finest mesh. The "exact" Euler solution should give zero drag. The 5-wave model, restarted from the grid-aligned solution with θ'_d frozen, gives a far better prediction of the drag than the grid-aligned scheme for all three grids. Entropy contours for both methods on the coarsest and finest meshes, figures 6(a) and (b) and 7(a) and (b), indicate significantly lower entropy production over the airfoil surface using the 5-wave model. (Contour values plotted are 0.001 through 0.03 in steps of 0.001 for all four figures.)

It is believed that the difference in entropy levels is due to the different ways that the two models interpret the flow near the stagnation point of the airfoil. Near the stagnation point, the flow undergoes very rapid turning with relatively small changes in pressure. The grid-aligned model interprets this turning to be in part due to the action of + and − acoustic waves with nearly offsetting Δp's. Because the local flow is subsonic, the wavespeeds associated with each of these acoustic waves are of opposite sign, so the flux computed at interfaces near the leading edge is assigned a pressure which is too high or low by an amount Δp. This results in increased entropy generation. In contrast, the 5-wave model interprets the rapid turning near the stagnation point to be due primarily to the action of a $(\theta'_d + \pi/2)$ shear wave, which has no associated pressure jump across it. The entropy is lower as a consequence.

Second-order spatially accurate computations for both the 5-wave and the grid-aligned models entail extrapolating the left and right states at each interface from primitive variables in the grid-aligned directions. It should be noted at this point that, in general, second-order computations using the 5-wave model show only small improvement over grid-aligned computations. Shock waves that lie oblique to the grid are usually resolved with about the same thickness using both methods. Also, the amount of entropy generated over an airfoil in a subsonic Euler computation is of the same order for both the 5-wave and grid-aligned models.

However, a specific case where an advantage of the 5-wave model over the grid-aligned model is realized in a second-order computation is for viscous separated flow over a NACA 0012 airfoil at M = 0.5, $\alpha = 3°$, and Re = 5000. On even reasonably fine meshes, the grid-aligned scheme does a poor job since there is a detached shear layer emanating from about midchord which is not oriented with the grid. The shear is misinterpreted as a combination of shear and compression, with the end result of a distortion in the computed pressure. An example is shown in figure 8(a) for a computation on a 129 × 49 C-mesh with minimum spacing of 0.0004c and maximum outer boundary extent of 14c. Figure 8(b) shows results over the rear half of the airfoil using the 5-wave model with no limiting on θ'_d, restarted from the grid-aligned solution with θ'_d frozen. Here the odd-even point decoupling mentioned in the Monotonicity Analysis section can be seen. When θ'_d-limiting is employed, this decoupling is no longer evident and the pressure distortions in the shear layer are significantly reduced as shown in figure 8(c). (In each of these figures, contour values of 0.9 through 1.2 in steps of 0.005 are plotted.)

THREE-DIMENSIONAL MODEL

The extension of the grid-independent flux function to three dimensions is fairly straightforward. The flux per unit face area is given by (10), but now the five

waves are represented by

$$\hat{\mathbf{R}}_1 = \begin{bmatrix} 1 \\ \hat{u} + \hat{a}(c_x)'_d \\ \hat{v} + \hat{a}(c_y)'_d \\ \hat{w} + \hat{a}(c_z)'_d \\ \hat{H} + \hat{a}\hat{q}'_d \end{bmatrix} \qquad \hat{\mathbf{R}}_2 = \begin{bmatrix} 1 \\ \hat{u} - \hat{a}(c_x)'_d \\ \hat{v} - \hat{a}(c_y)'_d \\ \hat{w} - \hat{a}(c_z)'_d \\ \hat{H} - \hat{a}\hat{q}'_d \end{bmatrix} \qquad (42)$$

$$\hat{\mathbf{R}}_3 = \begin{bmatrix} 0 \\ -\hat{a}(c_x)'_d \\ -\hat{a}(c_y)'_d \\ -\hat{a}(c_z)'_d \\ -\hat{a}\hat{q}'_d \end{bmatrix} \qquad \hat{\mathbf{R}}_4 = \begin{bmatrix} 1 \\ \hat{u} \\ \hat{v} \\ \hat{w} \\ \frac{1}{2}(\hat{u}^2 + \hat{v}^2 + \hat{w}^2) \end{bmatrix} \qquad (43)$$

$$\hat{\mathbf{R}}_5 = \begin{bmatrix} 0 \\ -\hat{a}(\Delta r_1)'_d \\ -\hat{a}(\Delta r_2)'_d \\ -\hat{a}(\Delta r_3)'_d \\ -\hat{a}\{\hat{u}(\Delta r_1)'_d + \hat{v}(\Delta r_2)'_d + \hat{w}(\Delta r_3)'_d\} \end{bmatrix} \qquad (44)$$

where

$$\hat{q}'_d \equiv \hat{u}(c_x)'_d + \hat{v}(c_y)'_d + \hat{w}(c_z)'_d \qquad (45)$$

and

$$\begin{aligned} \Delta r_1 &\equiv ((c_x)^2 - 1)\Delta u + (c_x)(c_y)\Delta v + \\ &\quad (c_x)(c_z)\Delta w \\ \Delta r_2 &\equiv (c_y)(c_x)\Delta u + ((c_y)^2 - 1)\Delta v + \\ &\quad (c_y)(c_z)\Delta w \\ \Delta r_3 &\equiv (c_z)(c_x)\Delta u + (c_z)(c_y)\Delta v + \\ &\quad ((c_z)^2 - 1)\Delta w. \end{aligned} \qquad (46)$$

The variables c_x, c_y, and c_z represent the components of the unit normal direction vector $\vec{n}$ in the x, y, and z directions, respectively. They can be written:

$$\begin{aligned} c_x &\equiv \cos\theta\cos\psi \\ c_y &\equiv \sin\theta\cos\psi \\ c_z &\equiv \sin\psi, \end{aligned} \qquad (47)$$

where the angles θ and ψ define a direction in three dimensions as depicted in figure 9. The velocity-difference direction $\vec{n}_d$, defined by the angles (θ_d, ψ_d), is obtained using

$$\begin{aligned} \theta_d &= \tan^{-1}\left(\frac{\Delta v}{\Delta u}\right) \\ \psi_d &= \tan^{-1}\left(\frac{\Delta w * \text{sign}(\Delta u)}{\sqrt{\Delta u^2 + \Delta v^2}}\right). \end{aligned} \qquad (48)$$

The angles are each defined from $-\frac{\pi}{2}$ to $\frac{\pi}{2}$. As in two dimensions, the direction of wave propagation is frozen as $\vec{n}'_d$ in order to eliminate nonlinear feedback in the solution.

The vector of wavestrengths is given by

$$\hat{\mathbf{\Omega}} = \begin{bmatrix} \frac{\Delta p}{2\hat{a}^2} + \frac{\beta\hat{\rho}}{2\hat{a}}\Delta q'_d \\ \frac{\Delta p}{2\hat{a}^2} - \frac{\beta\hat{\rho}}{2\hat{a}}\Delta q'_d \\ (\beta - 1)\frac{\hat{\rho}}{\hat{a}}\Delta q'_d \\ \frac{1}{\hat{a}^2}\left(\hat{a}^2\Delta\rho - \Delta p\right) \\ \frac{\hat{\rho}}{\hat{a}} \end{bmatrix}, \qquad (49)$$

and β is defined by

$$\beta \equiv \min\left[\max\left\{\left(\frac{\Delta p/(\hat{\rho}\hat{a})}{\Delta q'_d}\right)^2, .05\right\}, 1\right], \qquad (50)$$

where

$$\Delta q'_d \equiv \Delta u(c_x)'_d + \Delta v(c_y)'_d + \Delta w(c_z)'_d. \qquad (51)$$

All of the waves except for the shear wave represented by $\hat{\mathbf{R}}_3$ have wavespeeds in the $\vec{n}'_d$-direction. The direction of propagation of the shear wave $\hat{\mathbf{R}}_3$ is taken normal to the plane spanned by $\vec{V}_L$ and $\vec{V}_R$. This direction is chosen so that the model is able to sharply capture oblique shear waves through which the velocity undergoes rotation. Its derivation is discussed in greater detail in reference 3. The velocity $\bar{u}_s$ of this shear wave is identically zero when the direction of wave-propagation is not frozen. When the direction is frozen, then $\bar{u}'_s$, although small, is no longer necessarily zero. It is given by

$$\bar{u}'_s = \hat{u}(c_x)'_s + \hat{v}(c_y)'_s + \hat{w}(c_z)'_s, \qquad (52)$$

where $(c_x)'_s$, $(c_y)'_s$, and $(c_z)'_s$ are the components of the frozen shear-propagation direction in the three coordinate directions.

Finally, the components of the wavespeeds of all five waves in the grid-normal direction are written:

$$\begin{aligned} \hat{\lambda}_1 &= (\hat{q}'_d + \hat{a})\{(c_x)'_d(c_x)_g + (c_y)'_d(c_y)_g + \\ &\quad (c_z)'_d(c_z)_g\} \\ \hat{\lambda}_2 &= (\hat{q}'_d - \hat{a})\{(c_x)'_d(c_x)_g + (c_y)'_d(c_y)_g + \\ &\quad (c_z)'_d(c_z)_g\} \\ \hat{\lambda}_3 &= \bar{u}'_s\{(c_x)'_s(c_x)_g + (c_y)'_s(c_y)_g + (c_z)'_s(c_z)_g\} \\ \hat{\lambda}_4 &= \hat{q}'_d\{(c_x)'_d(c_x)_g + (c_y)'_d(c_y)_g + (c_z)'_d(c_z)_g\} \\ \hat{\lambda}_5 &= \hat{q}'_d\{(c_x)'_d(c_x)_g + (c_y)'_d(c_y)_g + (c_z)'_d(c_z)_g\}. \end{aligned} \qquad (53)$$

A monotonicity analysis in three dimensions proceeds in much the same way as the analysis in two dimensions. However, for simplicity it is assumed that the shear-wave speed associated with $\hat{\mathbf{R}}_3$ is identically zero (which would be exactly true if the wave-propagation direction was never frozen).

Results are plotted as allowable $|\vec{n}'_d - \vec{n}_f|$ vs. $|\vec{n}_g - \vec{n}_f|$, for various ϕ_p, where ϕ_p is the angle between the plane defined by the vectors $(\vec{n}_g, \vec{n}_f)$ and the plane defined by the vectors $(\vec{n}'_d, \vec{n}_f)$. The quantities within the absolute value signs indicate an angular difference between two vectors. When plotted this way, results are independent of the flow vector $\vec{n}_f$.

A result is given in figures 10(a) through (c) for M = 3, and $\beta = 1$. Figure 10(a) shows results for the cases

when $\phi_p < 15°$. The allowable region for monotonicity looks very similar to the two-dimensional region at these same conditions (see figure 2(a)). It includes the grid-aligned wave model $\vec{n}_d' = \vec{n}_g$. Notice that for the three-dimensional case, in contrast to two dimensions, the absolute value of the angular differences are plotted so that only positive differences are given. This is done because of the difficulty associated with assigning a positive or negative angular difference in three dimensions. When $15° < \phi_p < 30°$, the plot of figure 10(b) results. Here, the monotone region is similar to figure 10(a) except that the grid-aligned model is no longer representable. When $30° < \phi_p < 45°$, the monotonicity region diminishes significantly in size, as shown in figure 10(c). Finally, when $45° < \phi_p < 90°$, *no* region is monotone, according to this analysis.

A specific example is taken from this case. Referring to figures 10(a) through (c), when $|\vec{n}_g - \vec{n}_f| \approx 75°$, the allowable $|\vec{n}_d' - \vec{n}_f|$ goes from about 25° to 75° for $\phi_p < 15°$, from about 25° to 65° for $15° < \phi_p < 30°$, and from about 35° to 45° for $30° < \phi_p < 45°$. A sketch is first drawn in figure 11(a) of the $\vec{n}_f$ vector and the $\vec{n}_g$ vector, separated by 75°, with the allowable $\vec{n}_d'$-directions in the $(\vec{n}_g, \vec{n}_f)$-plane $(\phi_p = 0°)$ indicated by shading. Next, in figure 11(b), the allowable $\vec{n}_d'$-directions in all three dimensions are indicated by including the results from the cases when the $(\vec{n}_d', \vec{n}_f)$-plane differs significantly from the $(\vec{n}_g, \vec{n}_f)$-plane.

A second case using $M = 0.3$, $\beta = 1$ is shown in figure 12 for $\phi_p = 0°$. When $\phi_p > 0°$, there are no regions of monotonicity. This figure indicates (as did figure 2(b) for two dimensions) that only the grid-aligned method is monotone at these subsonic conditions. However, it is believed that this constraint, as well as the constraints imposed when the flow is supersonic, can be relaxed somewhat in practice. Although an empirical limiting method has not been devised for three-dimensional flow due to its inherent complexity, it is believed that a successful method would be patterned much the same as the method currently employed for two dimensions.

A sample three-dimensional Euler result is given for flow through a channel with a ramp. This case was first performed by Parpia.[4] The geometry is shown in figure 13. Computations are performed on a $41 \times 17 \times 17$ grid at an inflow Mach number of 2.8. Pressure contours in the $i = 1$ and $i = 17$ planes (far and near walls) are shown in figures 14(a) and (b) and 15(a) and (b) using first-order spatial discretization. The 5-wave model is seen to yield sharper shocks than the grid-aligned model for this case.

CONCLUSIONS

A monotonicity analysis is performed for a multidimensional flux function applied to the Euler equations. From the analysis, a limiting procedure is devised for two-dimensional flow which yields solutions with reduced oscillatory behavior while still maintaining sharper resolution of flowfield discontinuities than

the grid-aligned flux function. The effect of the limiting is demonstrated for the case of supersonic channel flow with a ramp. The limited model is also applied to a subsonic Euler computation over an airfoil and a separated viscous flow Navier-Stokes computation over an airfoil. First-order accurate results for the subsonic airfoil flow yield lower entropy and hence more accurate drag predictions than the grid-aligned model. In the Navier-Stokes case, pressure distortions computed in the separated region over the airfoil by the grid-aligned model are reduced by the grid-independent model. The model is also extended to three dimensions, and a monotonicity analysis shows the behavior to be similar to the two-dimensional case. First-order results for a three-dimensional channel flow with a ramp give sharper resolution of oblique shocks than the grid-aligned model. A limiting procedure is not developed for the three-dimensional model.

REFERENCES

1. Roe, P., "Approximate Riemann Solvers, Parameter Vectors, and Difference Schemes," JCP, 43, 1981, pp. 357-372.

2. Rumsey, C., Van Leer, B., Roe, P., "A Grid-Independent Approximate Riemann Solver with Applications to the Euler and Navier-Stokes Equations," AIAA Paper 91-0239, 1991.

3. Rumsey, C., "Development of a Grid-Independent Approximate Riemann Solver," Ph.D. Thesis, University of Michigan, 1991 (to appear).

4. Parpia, I., private communication, 1990.

5. Rumsey, C., Anderson, W., "Parametric Study of Grid Size, Time Step, and Turbulence Model on Navier-Stokes Computations Over Airfoils," Validation of Computational Fluid Dynamics, AGARD-CP-437, Vol. 1, 1988, pp. 5-1 - 5-19.

6. Godunov, S., "Finite Difference Method for Numerical Computation of Discontinuous Solutions of the Equations of Fluid Dynamics," Matematicheskii Sbornik 47, No. 3, 1959, p.271, Cornell Aeronautical Lab (CALSPAN) translation.

7. Levy, D., Powell, K., Van Leer, B., "An Implementation of a Grid-Independent Upwind Scheme for the Euler Equations," AIAA Paper 89-1931-CP, 1989.
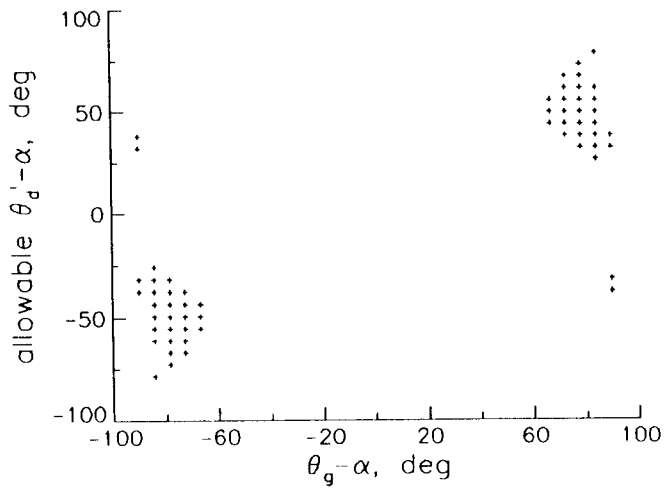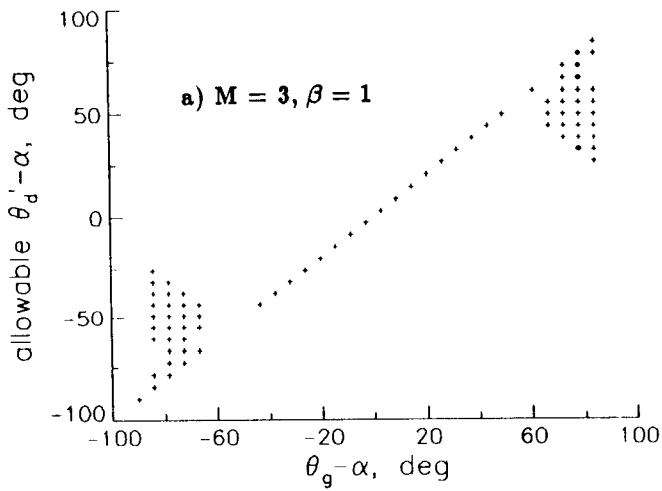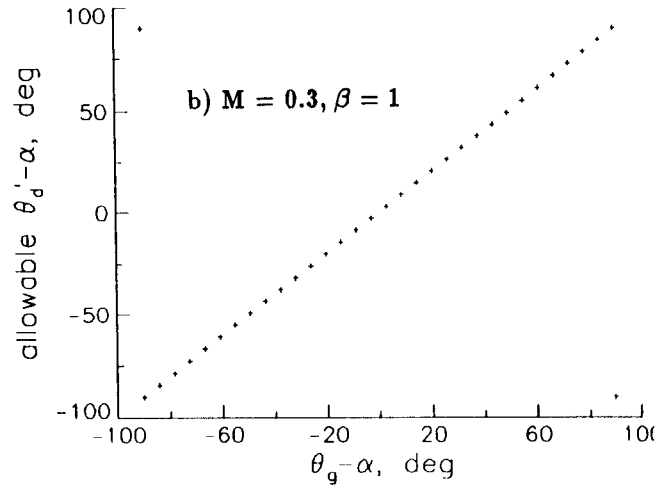
a) monotonicity regions
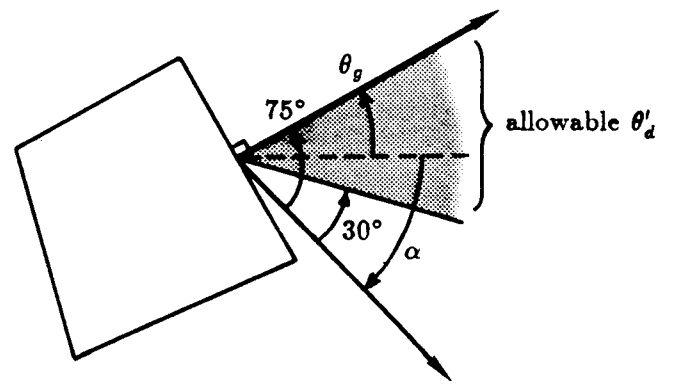
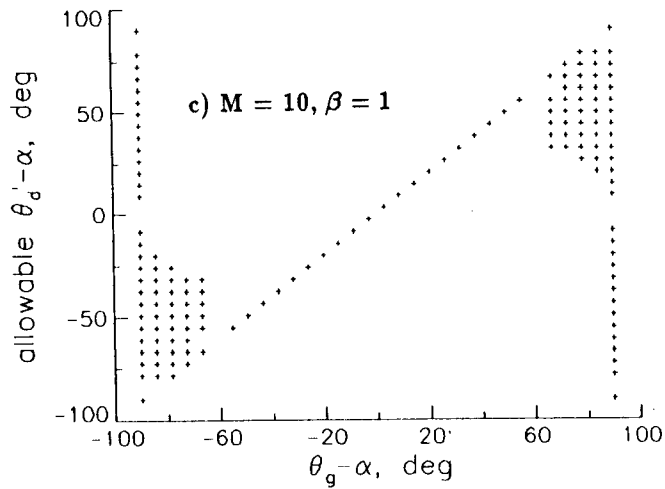b) allowable θ'_d when $\theta_g - \alpha = 75°$

Fig. 1 Monotonicity for M = 3, β = 0.95

a) M = 3, β = 1

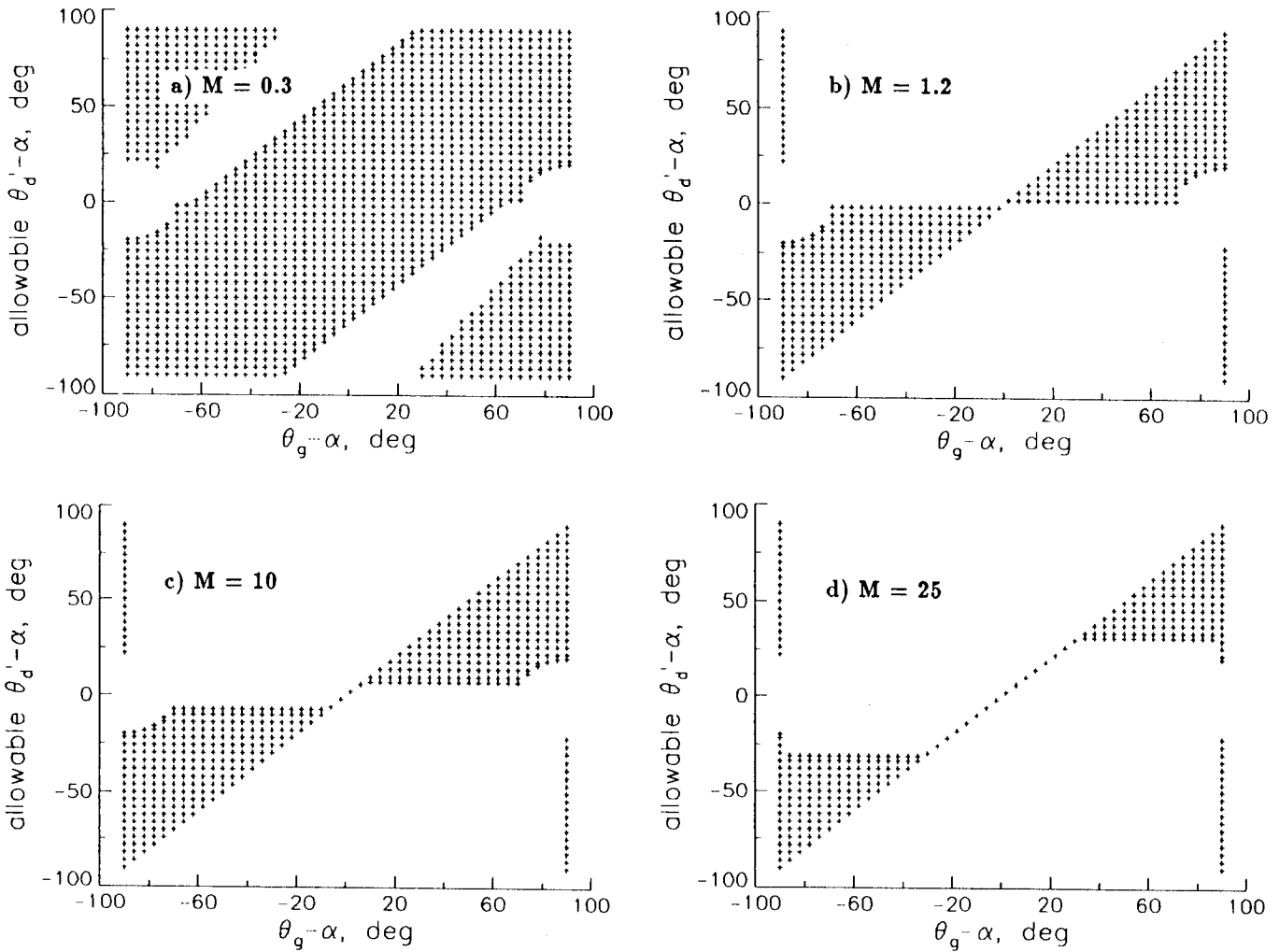b) M = 0.3, β = 1

c) M = 10, β = 1

Fig. 2 Monotonicity regions
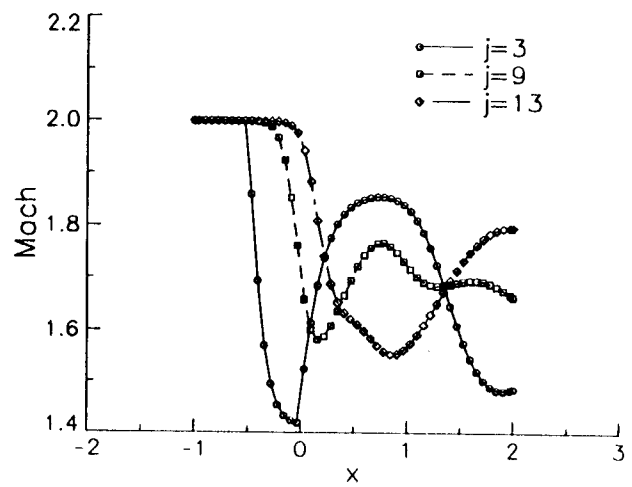
Fig. 3 Empirically-determined monotonicity regions

a) grid-aligned model
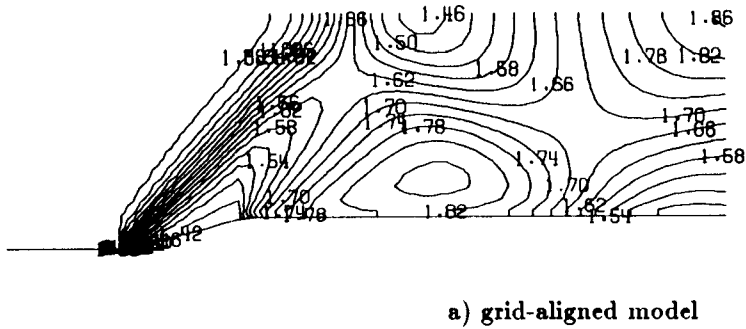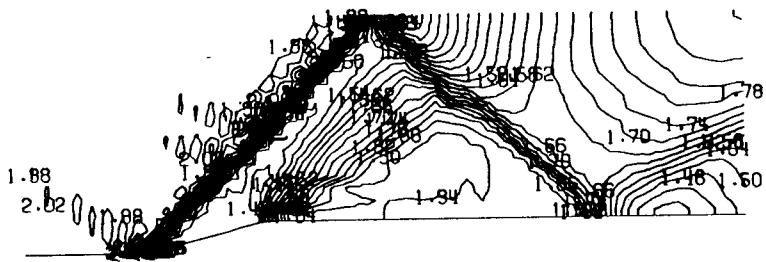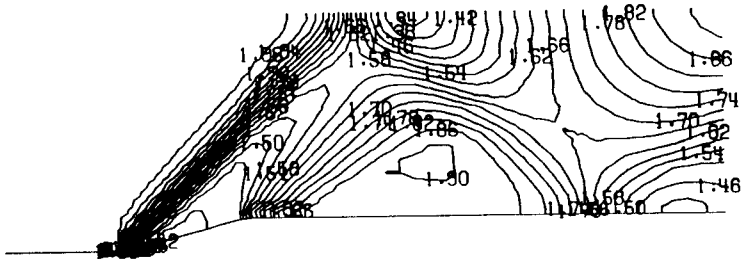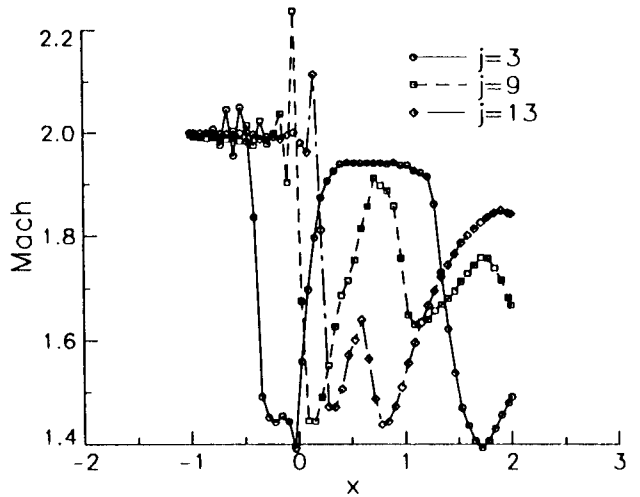
Fig. 4 Mach contours and Mach number values, channel
flow, M = 2, 1st-order

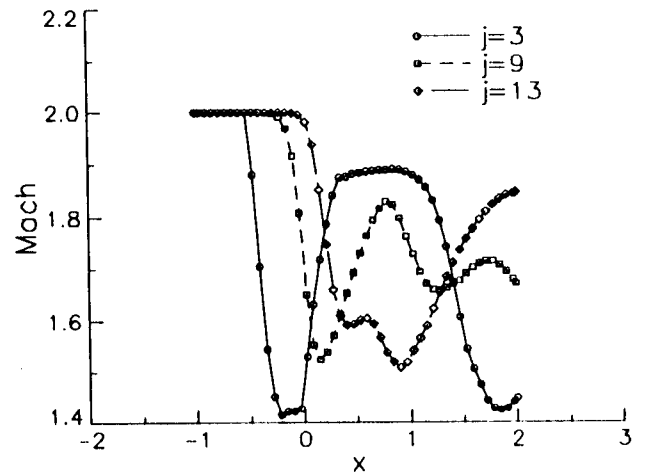b) 5-wave model (θ'_d not limited)
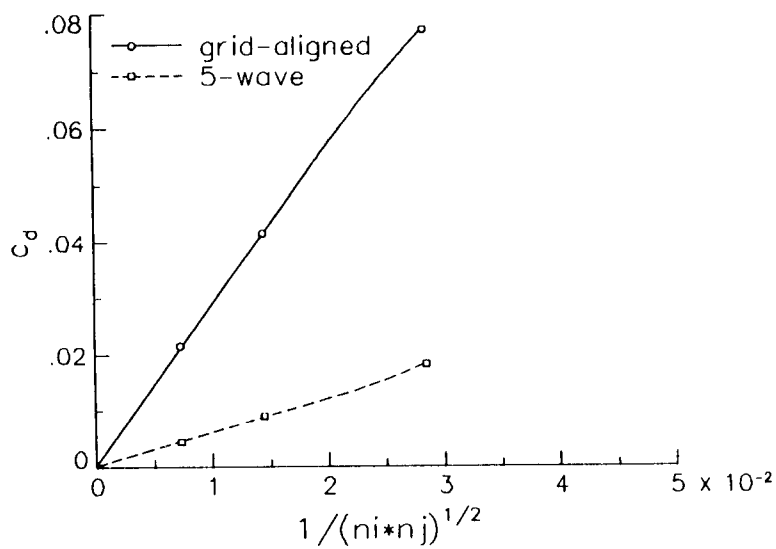
c) 5-wave model (θ'_d-limited)

Fig. 4 Continued

Fig. 5 Grid convergence study, NACA 0012, M = 0.3,
$\alpha = 1°$, 1st-order
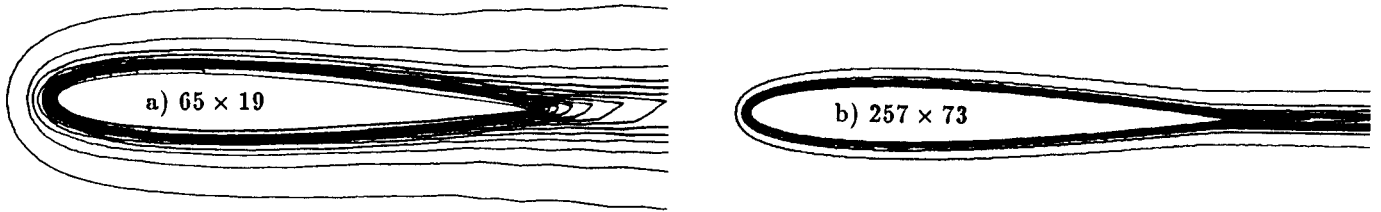
Fig. 6 Entropy contours, NACA 0012, M = 0.3, α = 1°,
1st-order, grid-aligned model
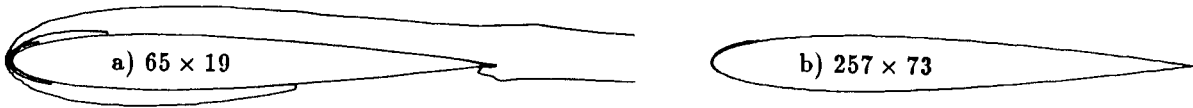
Fig. 7 Entropy contours, NACA 0012, M = 0.3, α = 1°,
1st-order, 5-wave model
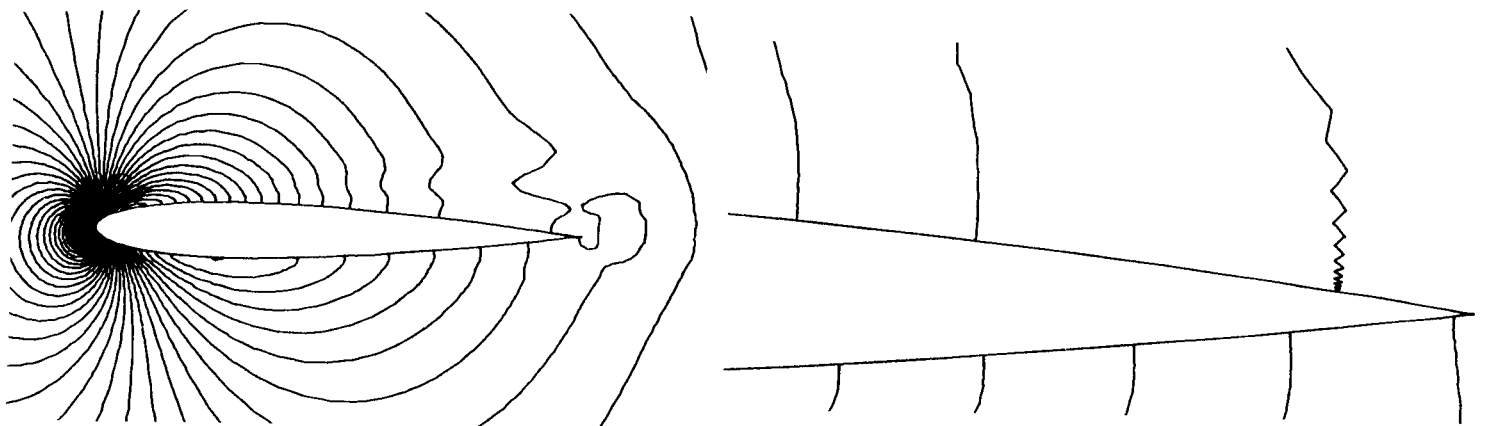
a) grid-aligned model

b) 5-wave model (θ'_d not limited)
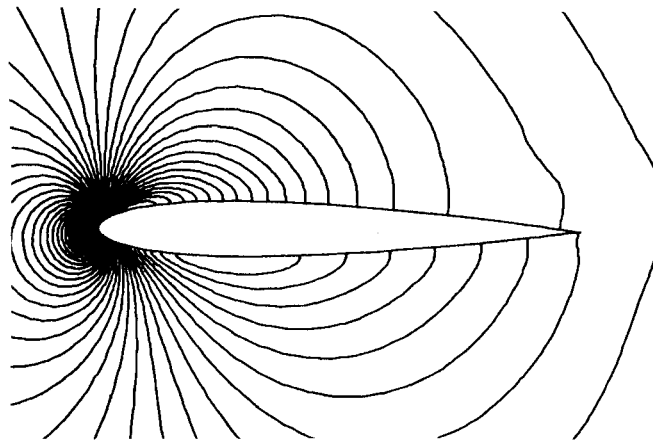
c) 5-wave model (θ'_d-limited)

Fig. 8 Pressure contours, NACA 0012 airfoil, M = 0.5,
α = 3°, Re = 5000, 2nd-order Navier-Stokes
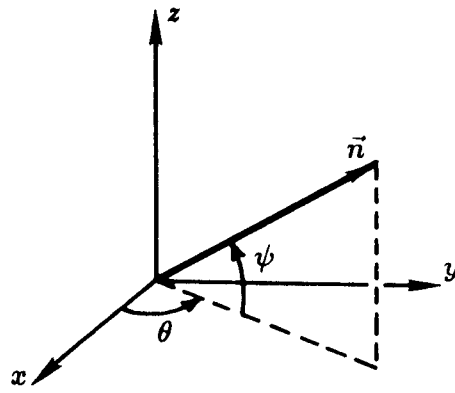
Fig. 9 3-D angle definition
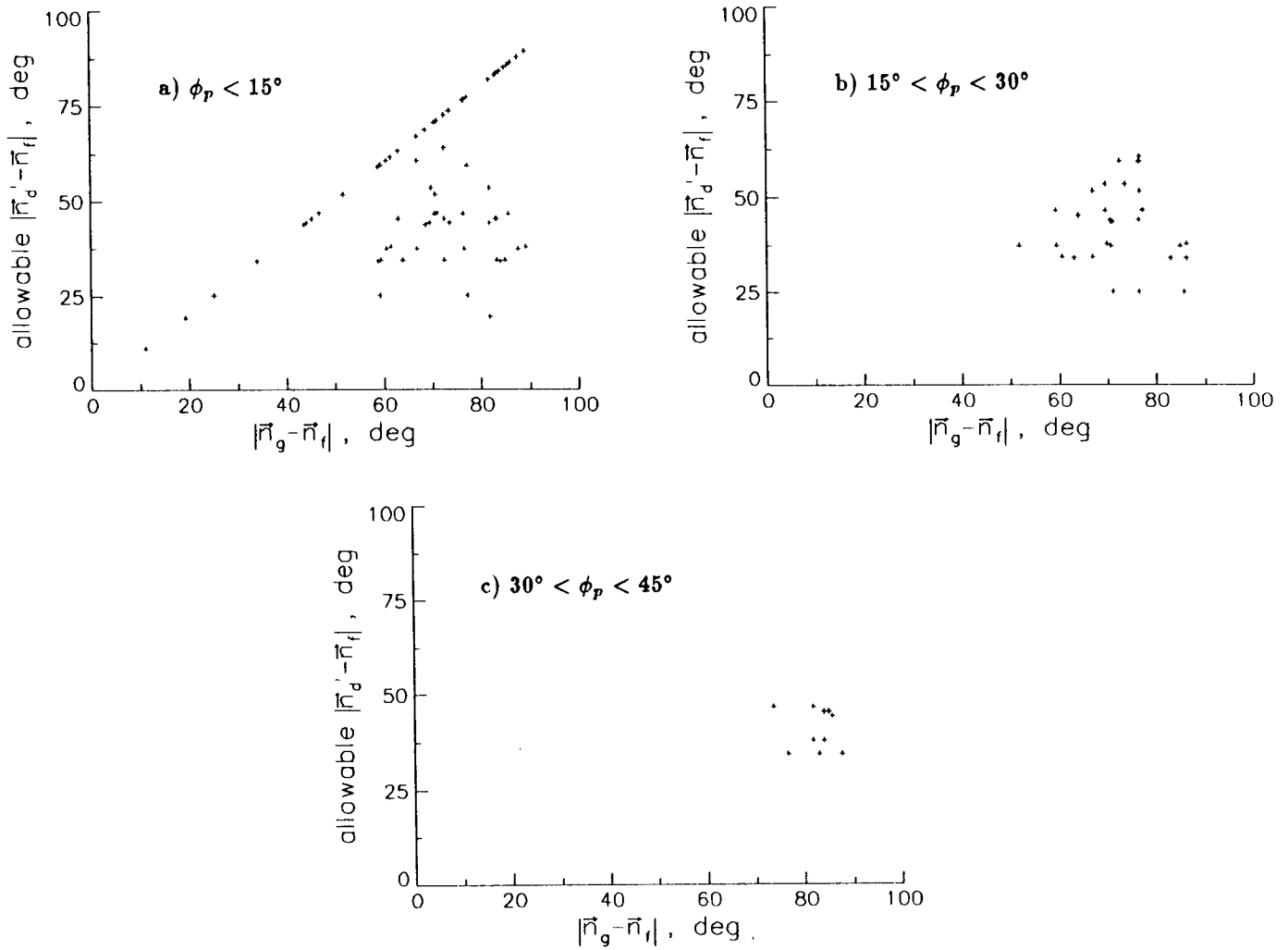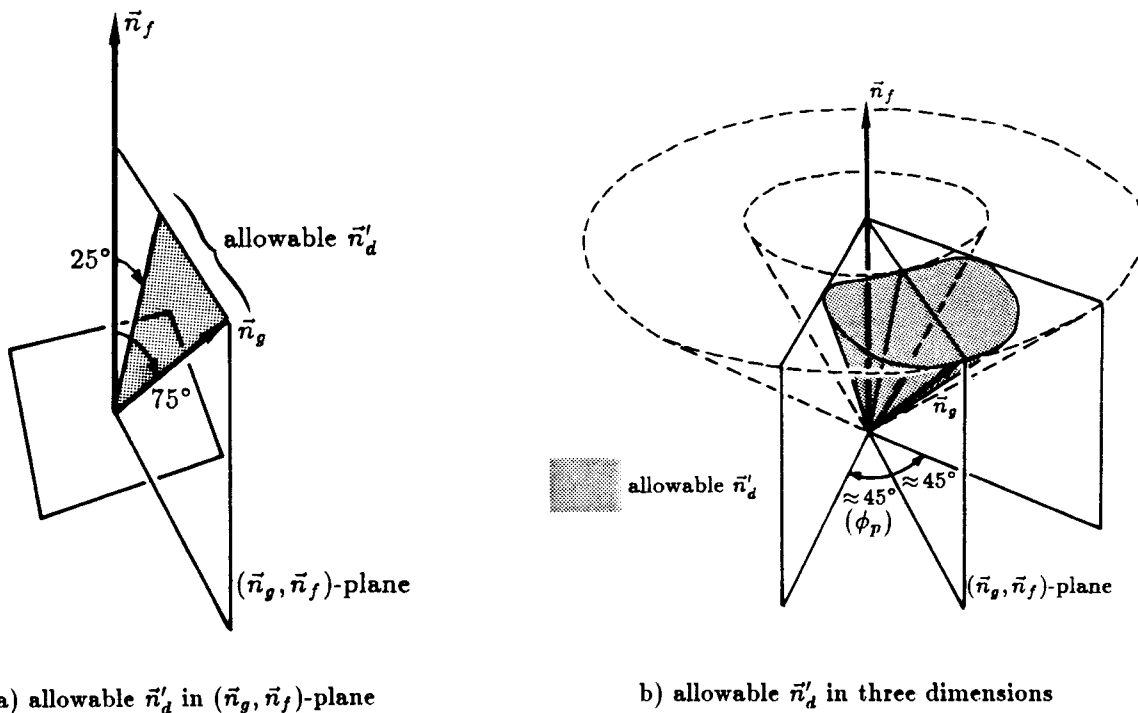

Fig. 10 Monotonicity regions, M = 3, $\beta = 1$

a) allowable $\vec{n}_d'$ in $(\vec{n}_g, \vec{n}_f)$-plane

b) allowable $\vec{n}_d'$ in three dimensions

Fig. 11 Monotonicity for M = 3, $\beta = 1$; allowable $\vec{n}_d'$ when
$|\vec{n}_g - \vec{n}_f| = 75°$
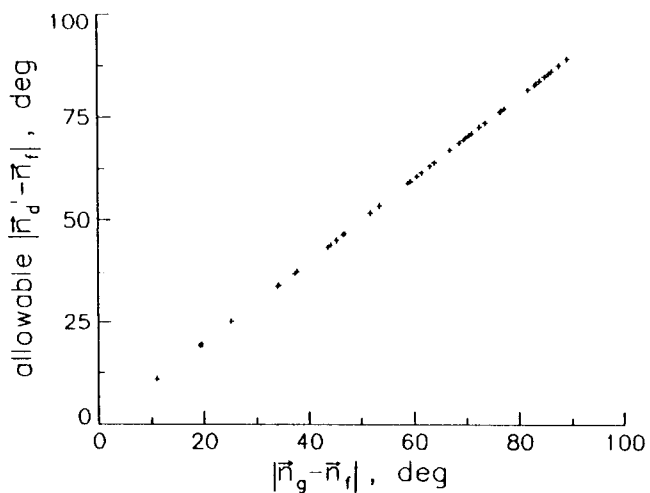
Fig. 12 Monotonicity region, M = 0.3, $\beta = 1$, $\phi_p = 0°$
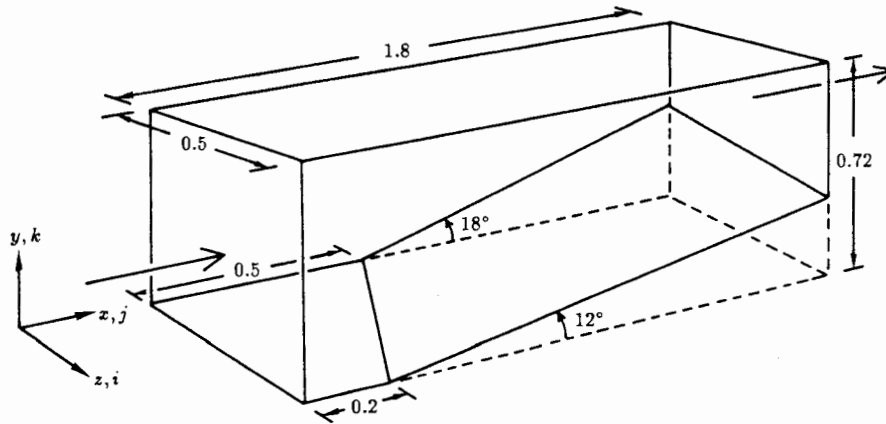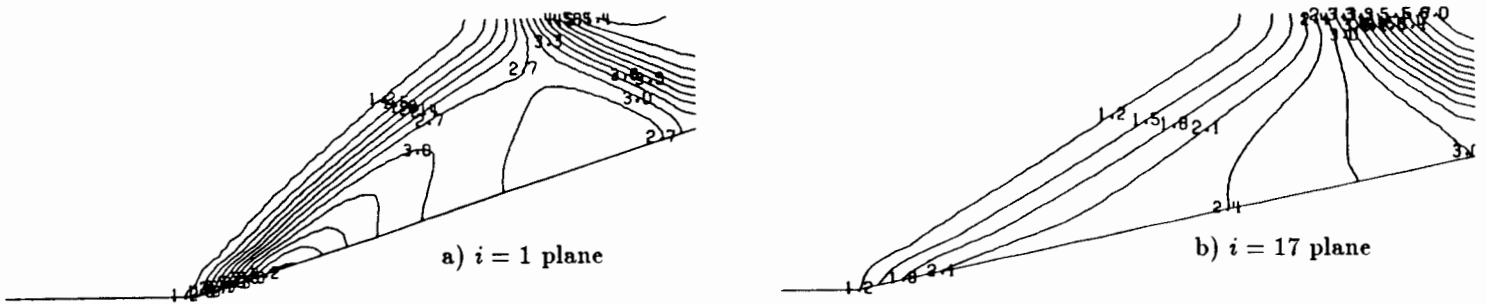
45

Fig. 13 Geometry of 3-D channel

a) $i = 1$ plane

b) $i = 17$ plane

Fig. 14 Pressure contours, 3-D channel flow, M = 2.8, 1st-order, grid-aligned model
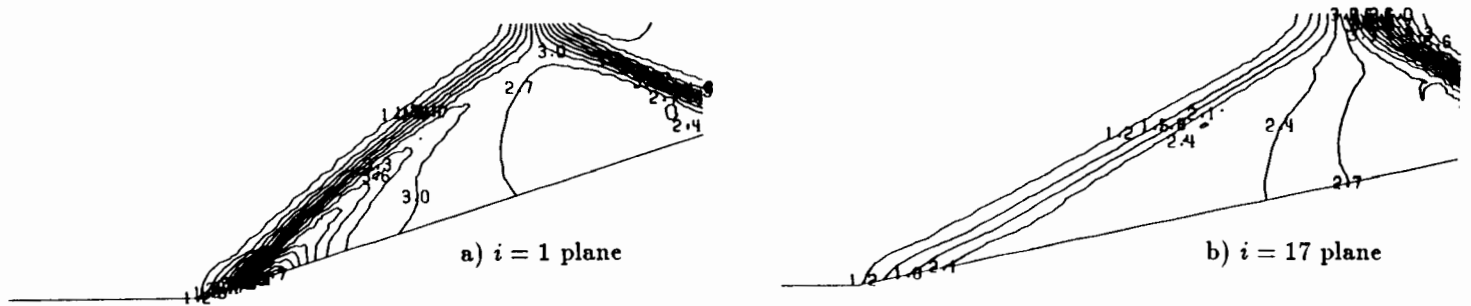

a) $i = 1$ plane

b) $i = 17$ plane

Fig. 15 Pressure contours, 3-D channel flow, M = 2.8, 1st-order, 5-wave model